Journal of Power Sources 195 (2010) 1926–1935

Contents lists available at ScienceDirect

Journal of Power Sources

journal homepage: www.elsevier.com/locate/jpowsour

# Evaluating the impact of enhanced anode CO tolerance on performance of proton-exchange-membrane fuel cell systems fueled by liquid hydrocarbons

Jenny E. Hu [a], Joshua B. Pearlman [a], Gregory S. Jackson [a,*], Christopher J. Tesluk [b]

[a] Dept. of Mechanical Engineering, University of Maryland, College Park, MD 20742, USA
[b] Ballard Power Systems, Burnaby, British Columbia V5J 5J8, Canada

ARTICLE INFO

*Article history:*
Received 30 July 2009
Received in revised form
18 September 2009
Accepted 30 September 2009
Available online 9 October 2009

*Keywords:*
PEM fuel cell
CO tolerance
Hydrocarbon reforming
PROx reactor

ABSTRACT

Recent advances in anode electrocatalysts for low-temperature PEM fuel cells are increasing tolerance for CO in the $H_2$-rich anode stream. This study explores the impact of potential improvements in CO-tolerant electrocatalysts on the system efficiency of low-temperature Nafion-based PEM fuel cell systems operating in conjunction with a hydrocarbon autothermal reformer and a preferential CO oxidation (PROx) reactor for CO clean-up. The incomplete $H_2$ clean-up by PROx reactors with partial CO removal can present conditions where CO-tolerant anode electrocatalysts significantly improve overall system efficiency. Empirical fuel cell performance models were based upon voltage–current characteristics from single-cell MEA tests at varying CO concentrations with new Pt–Mo alloy reformate-tolerant electrocatalysts tested in conjunction with this study. A system-level model for a liquid-fueled PEM fuel cell system with a 5 kW full power output is used to study the trade-offs between the improved performance with decreased CO concentration and the increased penalties from the air supply to the PROx reactor and associated reduction in $H_2$ partial pressures to the anode. As CO tolerance is increased over current state-of-the-art Pt alloy catalysts, system efficiencies improve due primarily to higher fuel cell voltages and to a lesser extent to reductions in parasitic loads. Furthermore, increasing CO tolerance of anode electrocatalysts allows for the potential for reduced system costs with minimal efficiency penalty by reducing PROx reactor size through reduced CO conversion requirements.



## 1. Introduction

Expanding the market for proton-exchange-membrane (PEM) fuel cell systems, specifically for portable/mobile applications involving liquid hydrocarbon fuels, requires integration of a fuel reformer and associated balance of plant with the fuel cell stack. For low-temperature Nafion-based PEM fuel cells, integration with hydrocarbon fuel processing requires near-complete removal of CO from the reformate stream when the stack employs conventional Pt-based anode electrocatalysts. The need for hydration of the Nafion membrane requires operating temperatures below 90 °C at typical PEM fuel cell pressures. At such temperatures, pure Pt electrocatalysts as well as commercial PtRu anode electrocatalysts cannot effectively oxidize CO at concentrations above 100 ppm in the anode without unacceptable losses in current density at typical PEMFC operating voltages (0.6–0.8 V).

Current CO clean-up strategies for linking conventional low-temperature PEM fuel cell stacks with hydrocarbon reformers greatly increase the overall system size and complexity because of high temperatures in the fuel processor and the need for heat exchangers and reactors to cool the reformate, clean-up and burn the CO in the reformate, and capture the necessary water for running the reformer, either as a full endothermic steam reformer or an autothermal reformer. Such a system with an autothermal reformer is illustrated in the process schematic in Fig. 1, which shows a system that relies on a preferential CO oxidation (PROx) reactor for clean-up of the reformate. Besides the PROx reactor [1,2], other approaches considered for reformate CO removal include pressure-swing absorption (PSA) reactors [3] and Pd-based membrane purifiers [4,5]. The latter two approaches provide near-complete CO elimination, whereas the PROx reactor only provides partial clean-up. However, the PROx system avoids the penalties of including two large reactors and the regeneration process associated with PSA or the increased parasitic loads associated with high-pressure reformer operation required by Pd-based membranes. Furthermore, a PROx system has flexibility in that as anode electrocatalysts are developed with improved CO tolerance, the requirements on the PROx reactor – in terms of CO conversion and CO selectivity – may be reduced. This study utilizes a system model to explore how improved anode electrocatalysts with

* Corresponding author. Tel.: +1 301 405 2368; fax: +1 301 405 2025.
*E-mail address:* gsjackso@umd.edu (G.S. Jackson).

0378-7753/$ – see front matter © 2009 Elsevier B.V. All rights reserved.
doi:10.1016/j.jpowsour.2009.09.066

**Nomenclature**

| | |
|---|---|
| $A_{cell}$ | geometric area of single electrochemical cell in fuel cell stack ($cm^2$) |
| $F$ | Faraday's constant = 96,485 (C gmol electrons$^{-1}$) |
| $h_{H_2,comb}$ | lower enthalpy of combustion of $H_2$ (J kg$^{-1}$) |
| $h_{HC,comb}$ | lower enthalpy of combustion of hydrocarbon (J kg$^{-1}$) |
| $i$ | average effective current density per unit area in the fuel cell stack (A cm$^{-2}$) |
| $\dot{m}_{H_2,anode,in}$ | mass flow rate of $H_2$ into the anode (kg s$^{-1}$) |
| $\dot{m}_{HC,in}$ | mass flow rate of hydrocarbon into fuel reformer (kg s$^{-1}$) |
| $n_{cells}$ | number of electrochemical cells in fuel cell stack |
| $O/C$ | oxygen (from $O_2$) to carbon (from fuel) atomic ratio in fuel reformer inlet |
| $S/C$ | steam to carbon (from fuel) ratio in fuel reformer inlet |
| $T_{amb}$ | ambient temperature (°C or K) |
| $T_{WGS,out}$ | water-gas-shift outlet temperature (K) |
| $V_{cell}$ | voltage across an individual electrochemical cell in stack (V) |
| $\bar{W}_{H_2}$ | molecular weight of $H_2$ (g gmol$^{-1}$) |
| $\dot{W}_{lost}$ | parasitic power lost due to balance of plant components and DC–AC inverter (W) |
| $\dot{W}_{net}$ | net electrical power out (W) |
| $\varepsilon_{H_2}$ | fraction of anode inlet $H_2$ utilized in stack |
| $\eta_{BOP}$ | effective efficiency associated with power delivered to power produced by stack |
| $\eta_{FC}$ | effective efficiency of fuel cell stack |
| $\eta_{FP}$ | effective efficiency of fuel processor and Pd alloy membrane purifier combined |
| $\eta_{th}$ | overall effective system efficiency |
| $\xi_{CO}$ | anode CO-tolerance factor as defined in Section 2 |

increased CO tolerance can impact the overall system performance of a hydrocarbon-fueled PEM fuel cell system utilizing a PROx reactor for CO clean-up.

Recent advances in nanoparticle catalyst synthesis have shown that controlled alloy and nano-structured electrocatalysts may allow PEM fuel cells to operate at relatively high current (and thus power) densities on $H_2$ streams with CO levels of a few hundred ppm or more, even at the low temperatures required for Nafion-based PEM fuel cells [6,7]. This study builds on recent testing of PEM fuel cell membrane electrode assemblies (MEAs), which show CO tolerance of PtMo and PtRu alloy anode electrocatalysts, with relatively stable operation at 100 ppm CO or more [8–10]. The advances in anode electrocatalyst design suggest that with a new generation of CO-tolerant electrocatalysts, the reduced losses in current density due to CO at typical operating voltages may allow for reduced reformate clean-up and simplify a PEM fuel cell system with hydrocarbon fuel processing for $H_2$ production. In general, the increased tolerance for CO in PEM fuel cell anodes reduces the need for $H_2$ purification and thereby the penalties in overall efficiency resulting from fuel processing/purification in hydrocarbon-fueled PEM fuel cell systems. There is value in studying the system impacts of improved CO tolerance in Nafion-based PEM fuel cells.

Modeling the hydrocarbon fuel processing, PROx reactor CO clean-up, PEM fuel cell stack, and the balance of plant presents significant challenges because of the complex significant thermal integration and mass flow recycling for recovering water in the system. Balance of plant components including air compressors/blowers, liquid pumps, and a radiator fan present parasitic loads to the system that will vary strongly with operating conditions, power loads, and individual component performance. For the high level analysis, integrated system models with lumped analysis for individual components [5,11–15] provide an effective means for evaluating system design and performance of complex integrated PEM fuel cell power plants with hydrocarbon fuel processors. These studies have been conducted with various fuel reforming and CO-removal systems. However to date, no system models have clearly examined the impact on system performance of increased CO-tolerance in PEM fuel cell stacks and associated reduction in purification requirements. Past studies with PROx reactors in the system have often assumed that the PROx is 100% effective or that the CO is reduced to sufficiently low concentrations entering the fuel cell stack that performance is unaffected [13].

The current study builds on previous work [15] which explored the implications of complete $H_2$ purification using Pd-based membranes in PEM fuel cell systems running on liquid hydrocarbon fuels. The system-level model, which performs iterative mass, species, and energy balances on the fuel processor, fuel cell stack, and balance of plant components, has been modified for this study to explore the effects of partial $H_2$ clean-up using preferential oxidation reactors (PROx) for partial CO removal. The model results explore how increasing CO tolerance of anode electrocatalysts reduces the parasitic penalties in terms of air supply and unwanted $H_2$ consumption for the PROx reactor and thereby improves the system performance. Empirical fuel cell performance models to predict the effects of CO concentrations on the fuel cell performance were based upon voltage–current characteristic from single-cell MEA tests at varying CO concentrations with new alloy reformate-tolerant electrocatalysts being developed at the University of Maryland [6]. This study provides a clear indication of how future advances in CO-tolerant anode electrocatalysts can impact system efficiencies and preferred operating conditions for hydrocarbon-fueled PEM fuel cell systems.

## 2. System model description

The system flow diagram and component integration for a hydrocarbon-fueled PEM fuel cell generator is illustrated in the schematic of Fig. 1. This paper focuses on this particular configuration, which integrates a PEM fuel cell stack with a liquid-fueled autothermal reformer (ATR) with a subsequent water-gas-shift (WGS) reactor and a PROx reactor with proper thermal management for $H_2$ purification. Additional balance of plant subsystems, which account for parasitic loads, are also illustrated in Fig. 1 with the dominant parasitic loads coming from the air compressors for the fuel processor, cathode air, and PROx reactor and from the radiator fan. Electric motors and inverters for power conversion are not shown in Fig. 1, but both are incorporated into the model with constant efficiencies of 90 and 93%, respectively.

Components for the cathode-side air supply, exhaust burning, cooling, and water recovery are similar to those presented in an earlier study with a similar modeling approach [15]. The key difference between the current and previously reported systems is the replacement of the Pd membrane purifier in the previous study with a PROx reactor and associated air compressor and heat exchanger to cool the PROx effluent before it enters the fuel cell. Furthermore, Pd membrane purification was integrated with the water-gas-shift reactor in the previous study, while the present system incorporates just the water-gas-shift reactor without a membrane, as shown in Fig. 1.

The fuel processor is an autothermal fuel reformer (ATR) operating on a model kerosene (or JP-8), represented as $C_{12}H_{23}$ [15]. The autothermal reformer is maintained at constant steam to carbon ($S/C = 1.6$) and oxygen to carbon ($O/C = 0.8$) ratios. This condition is

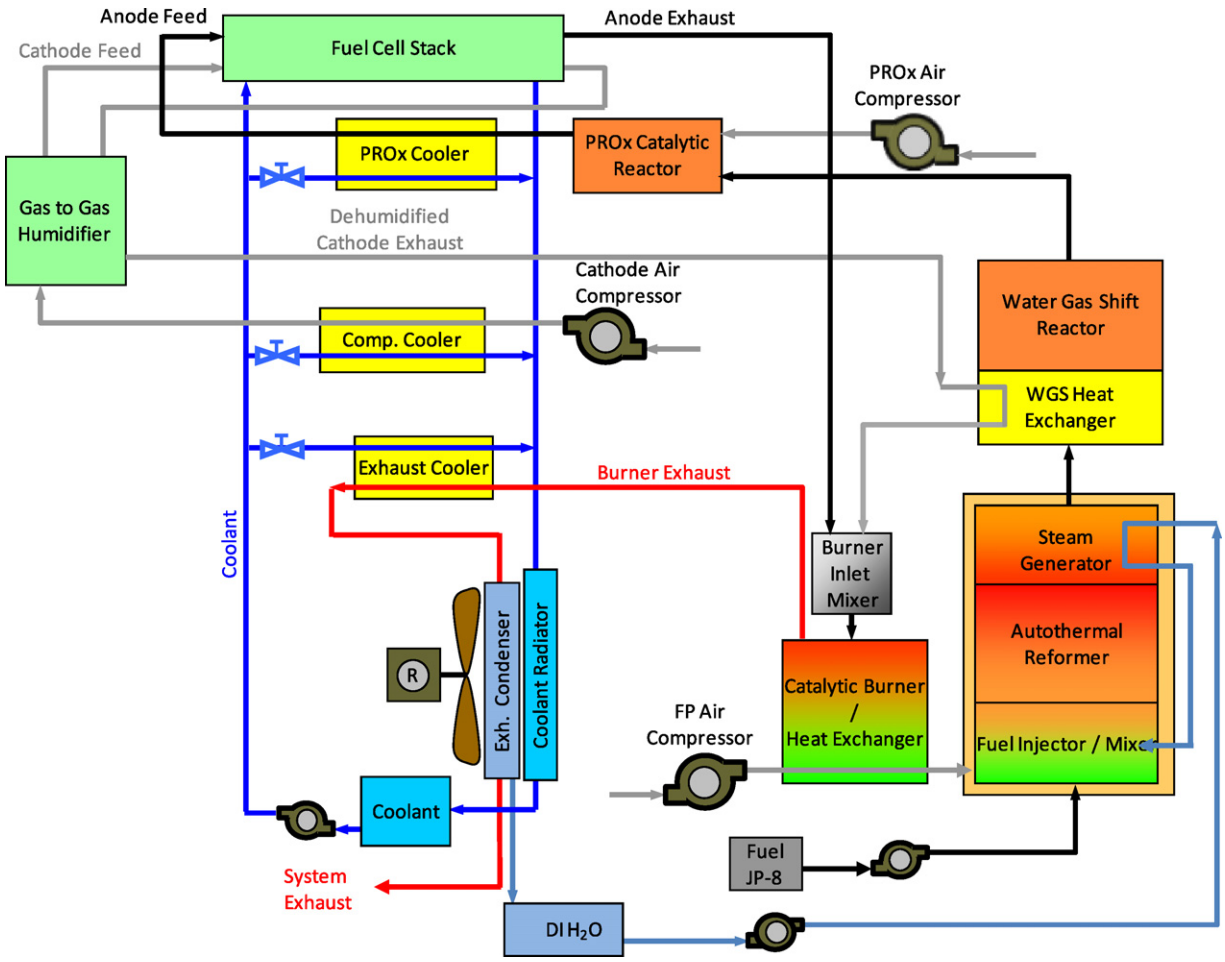


**Fig. 1.** Flow diagram showing schematic of hydrocarbon-fueled PEM fuel cell system modeled in this study with fuel processor, PROx reactor, catalytic exhaust burner, liquid-cooled fuel cell stack, and exhaust condenser for water recovery.

mildly exothermic and has been shown to have adequate O atoms to avoid significant carbon deposition in the reformer [16]. One key benefit in utilizing PROx for the CO clean-up is that the elimination of the Pd membrane purifier allows for a lower pressure (1.5 bar) in the ATR, which reduces parasitic loads associated with compressing the air for the reformer.

In the current study, the ATR is modeled by assuming outlet flows based on full fuel conversion and equilibration of the water-gas-shift reaction at the high outlet temperature. The outlet temperature and the equilibrium $H_2$, CO, $CO_2$, and $H_2O$ concentrations are found through an iterative solution of the coupled energy and species balances in the reactor. The energy balance includes some heat loss based on a constant convective heat transfer coefficient and a radiation loss fitted to liquid-fueled ATR experimental test results. With complete fuel conversion, all carbon in the reformate stream is assumed to exit as either CO or $CO_2$. The small percentage of $CH_4$ and other hydrocarbons (summed to <1.0% on a wet basis [17]) observed in ATR exhaust is not considered here. After the ATR effluent is cooled by an intermediate steam generator (for the reformer itself), the reformate passes through a WGS reactor, which is assumed to be sufficiently large to achieve equilibrium down to the exit temperature or to 300 °C, whichever is greater. The intermediate cooling between the ATR and the WGS reactor is critical to attaining lower exhaust-temperatures from the WGS and thus reduced CO concentrations to the PROx reactor and subsequently to the fuel cell stack. The WGS effluent is cooled through mixing with PROx compressor air before entering the PROx reactor at favorable temperatures to promote favorable CO conversion. The PROx reactor is modeled by assuming a fixed CO conversion and selectivity. For the current study, CO selectivity is generally held at a baseline value of 85%, which is consistent with advanced PROx reactors presented in the literature [18]. In this study here, model results explore the impact of varying PROx reactor CO selectivity on system performance. PROx CO conversion is generally fixed at a baseline of 95% although increased anode tolerance of CO encouraged studies looking at the effects on system performance of reduced CO conversion (80%) with a smaller, less expensive PROx reactor.

For the fuel cell stack, the model follows the earlier study where an empirical polarization curve is adapted from a study of a Ballard Power system fuel cell stack [19]. The open circuit voltage is shifted up or down based on changes in the Nernst potential with changes in reactant partial pressures and temperatures. However in this study, the pure $H_2$ voltage vs. current density ($V_{cell}$–$i$) curve is modified based upon the amount of CO in the anode feed. To this end, $V_{cell}$–$i$ curves for MEAs with relatively CO-tolerant PtMo alloy electrocatalysts are derived from experimental results with simulated reformate streams. Curves are obtained at 25, 50, 100, 250, 500, and 1000 ppm CO in $H_2$, at intervals of 50 mA $cm^{-2}$. These results (presented in the following section) are used to model the CO overpotentials as a percent drop from the reference hydrogen curve as a function of $i$. Linear interpolation is used between points and extrapolation beyond 1000 ppm. A CO-adjusted $V_{cell}$ is calculated for each desired current density and anode CO concentration from the PROx reactor. To further investigate the effects of CO tolerance, a CO-tolerance factor, $\xi_{CO}$, is introduced, which

reduces the CO penalty to that of a lower CO ppm value equal to the original CO ppm divided by the tolerance factor. For example, a CO-tolerance factor of 10 indicates that the polarization curve data obtained at 25 ppm is shifted to be effective at 250 ppm. As such, this provides a convenient means for investigating the system-level benefits of new advances in CO-tolerant anode electrocatalysts for the low-temperature PEM fuel cell systems relying on liquid-fuel reforming and PROx reactor CO clean-up.

For the remainder of the balance of plant (BOP) components, the heat exchanger, compressor, and pump models largely follow the earlier study. The reader is referred to that study for further details on heat transfer correlations for the heat exchangers and isentropic efficiency models for the compressors [15]. In the current study, more detail is given to modeling the high-flow-rate coolant loop, and the radiator fan power is taken from an experimental air flow rate vs. power curve. This helps to ensure that both the coolant pump and radiator fan parasitic loads are captured well in the model. In the PROx, cathode compressor, and exhaust heat exchangers as well as in the fuel cell stack, the model calculates the heat transfer required to bring the gas streams to a set target temperature, then solves for the coolant flow rate needed to provide the desired cooling. More detailed heat loss models are also implemented in the current study in order to examine temperature and thermal integration effects more closely. Heat losses are modeled in the WGS reactor, PROx reactor, and radiator as a combination of natural convection and radiation heat transfer based on the average temperature of the component and $T_{amb}$. Heat loss calculations assume a constant UA value for convective losses and a constant emissivity for radiative losses. The losses were determined by fitting calculations to heat loss estimates for testing of components in an effort to assemble a working prototype of a liquid-fueled PEM fuel cell generator.

As in the previous study, the model data is imported into MS Excel with a Visual Basic program running as a macro that determines steady-state operating conditions and system performance through a nested iterative sequence. The recycling of mass and heat flows, along with the feedback between system operating conditions and parasitic loads, requires such an iterative solution technique. The iterative loop is based upon stepping through each component and solving the non-linear energy balance and species balance equations. The overall system power demand is then used to recalculate fuel, air, and coolant flows, and associated parasitic loads for system operation. Fuel flow rate to the system is determined iteratively through a species balance between available $H_2$ exiting the PROx reactor and the demanded anode feed at the desired $H_2$ stoichiometry (1.3 for all cases here). The new flow rates thus are used to update the parasitic loads, and gross power demand for the fuel cell stack is calculated from the sum of net (i.e., usable) power demand and the parasitic loads.

## 3. Experiments for anode CO tolerance

CO performance of various electrocatalysts is characterized in 5.0 $cm^2$ single-cell membrane electrode assemblies (MEAs). The MEAs are fabricated using in-house manufactured PtMo alloy and core–shell nanoparticles [20] as well as 1:1 PtRu alloy from BASF Fuel Cell as the anode electrocatalyst. Catalyst ink has been prepared using 30 wt% catalyst on XC-72 carbon, mixed with a 5% Nafion solution and isopropyl alcohol. Ink is brushed onto a carbon cloth GDL to a total metal loading of 0.5 mg $cm^{-2}$. To form the MEA, the anode and cathode (0.5 mg $cm^{-2}$ Pt GDL from BASF Fuel Cell) are hot-pressed together with Nafion 212 membrane at 140 °C, 9 MPa, for 2 min. For comparison, complete MEAs with PtRu anodes and identical cathodes were also purchased from BASF.

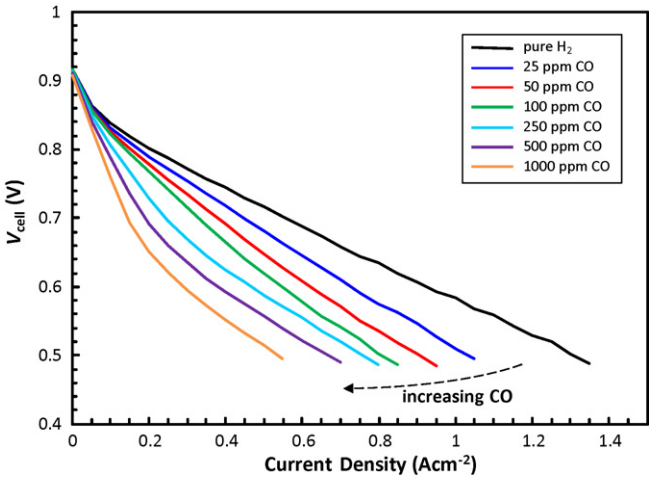


**Fig. 2.** Measured polarization curves in various CO concentrations (up to 1000 ppm) in the $H_2$ anode feed for a PEM fuel cell MEAs with ordered $Pt_{0.8}Mo_{0.2}$ alloy anode electrocatalyst. Cell and humidifier tanks were at 70 °C and 2.0 barg, and all flows were controlled at a fixed stoichiometry of 2.2.

A Scribner 850e test stand is used to provide humidified flows and record measurements. $H_2$/CO mixtures up to 1000 ppm are used as anode feeds, while air is the cathode oxidant. CO mixtures at 100 and 1000 ppm were obtained from Airgas and diluted using mass flow controllers. The cell is operated at 70–80 °C, with ~2.0 barg backpressure on both sides and with both humidifier bottles at the same temperature as the cell.

Polarization curves were measured for the different Pt–Mo and Pt–Ru anode electrocatalysts for a range of CO concentrations in $H_2$ anode feeds as reported elsewhere [21], and the ordered $Pt_{0.8}Mo_{0.2}$ alloy electrocatalyst showed superior CO tolerance as discussed in that previous work. Fig. 2 shows polarization curves from a MEA fabricated using the $Pt_{0.8}Mo_{0.2}$ alloy at 70 °C, with stoichiometries of 2.2 on both the anode and cathode inlet streams. The pure $H_2$ performance of the commercial BASF MEA with conventional PtRu anode electrocatalyst is superior to that of the MEA with the $Pt_{0.8}Mo_{0.2}$ alloy developed in association with this study, and this is due to non-optimized in-house MEA fabrication methods. Nonetheless, the superior CO tolerance of the $Pt_{0.8}Mo_{0.2}$ alloy anode electrocatalyst results in higher MEA performance (as indicated by $V_{cell}$–$i$ curves) than the commercial PtRu catalyst at all anode CO concentrations as low as 25 ppm, and the polarization curve improvements increase further with increasing anode CO concentrations as tested up to 1000 ppm. In general, CO oxidation, as indicated by the relatively rapid drop in the polarization resistance (or reduction in slope in the polarization curves in Fig. 2), begins at lower overpotentials on the $Pt_{0.8}Mo_{0.2}$ electrocatalysts than on the PtRu catalysts.

The performance of the $Pt_{0.8}Mo_{0.2}$ electrocatalysts at 70 °C, as shown by the curves in Fig. 2, is used to determine the CO penalty in the system model for this study. While the conditions in Fig. 2 are at higher total anode pressures (2 bar gauge) than those used in the model below (0.35 bar gauge), the CO penalty (due to competitive adsorption with $H_2$) is expected to only be a mild function with pressure and rather, a stronger function of CO mole fraction. As such, the penalties derived from these experiments should provide good assessment for the effects of anode CO mole fractions on the fuel cell electrochemical performance for the model.

## 4. Results and discussion

The current study does not explore the full system design space for the hydrocarbon-fueled PEM fuel cell system, but rather focuses

**Table 1**
Critical baseline system parameters.

| Parameter | Value |
|---|---|
| Critical baseline conditions | |
| Ambient conditions | |
| Temperature, $T_{amb}$ (K) | 303 |
| Relative humidity, $\phi_{amb}$ | 50% |
| Fuel cell conditions and properties | |
| Operating temperature, $T_{cell}$ (K) | 343 |
| Operating pressure, $P_{cell}$ (bar) | 1.35 |
| Pressure drop across stack at 1 A cm$^{-2}$ (bar) | 0.25 |
| Stoichiometric ratio of cathode air flow | 1.8 |
| Stoichiometric ratio of anode $H_2$ flow | 1.3 |
| Fraction of $H_2O$ produced in fuel cell to anode | 0.15 |
| Number of cells per stack | 75 |
| Stack membrane area per cell (cm$^2$) | 300 |
| Fuel reformer conditions | |
| Inlet oxygen to carbon ($O/C$) ratio | 0.8 |
| Inlet steam to carbon ($S/C$) ratio | 1.6 |
| Max. inlet temperature, $T_{ref,in,max}$ (K) | 773 |
| Min. pre-heater approach temperature (K) | 20 |
| Steam temperature out of generator (K) | 400 |
| Water-gas-shift reactor conditions | |
| Min. equilibrium temperature (K) | 575 |
| PROx reactor conditions | |
| Min. inlet temperature $T_{in}$ (K) | 440 |
| Balance of plant conditions | |
| Radiator coolant $T_{out}$ (K) | 333 |
| Min. exhaust condenser $\Delta T$ (K) | 10 |
| Electric inverter efficiency | 93% |
| Electric motor efficiency | 90% |

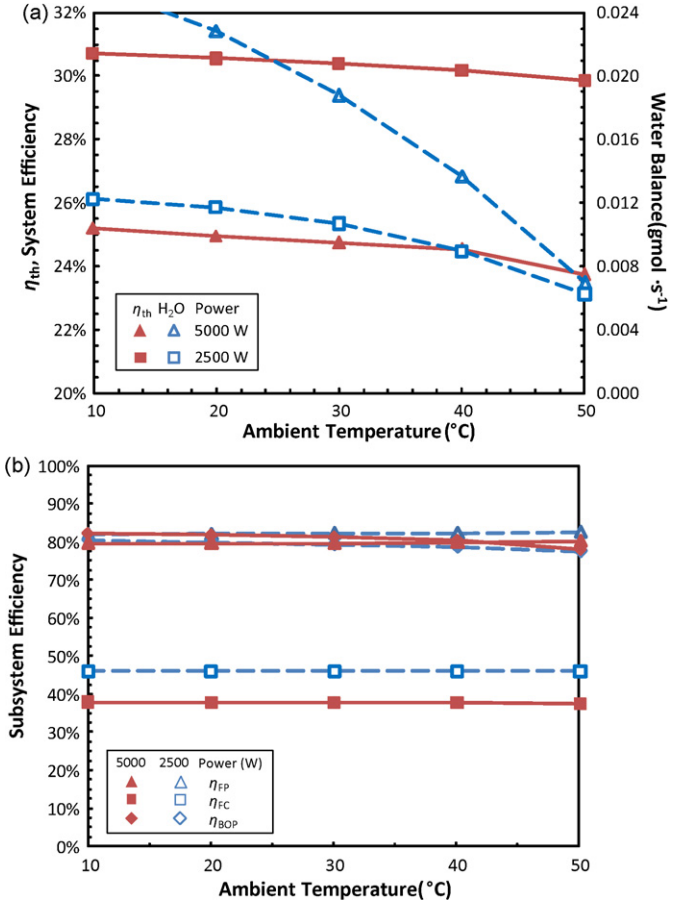


**Fig. 3.** PEM fuel cell performance vs. $T_{amb}$ at full and half power for a baseline CO tolerance and PROx reactor performance at 95% CO conversion and 0.85 CO selectivity: (a) total system efficiency and net water balance, and (b) subsystem efficiencies (fuel processor, fuel cell stack, and balance of plant).

on a baseline condition (with key parameters listed in Table 1) and variations from that, primarily related to PROx performance and anode CO tolerance. Of the parameters listed in Table 1, only ambient temperature is varied in this study. Other temperatures listed in the table simply indicate limits placed on system components such that unrealistic operating conditions will not be found by the solver and thus give false impressions regarding overall system performance. The system studied here, as illustrated by the process diagram in Fig. 1, is specified to operate at a full power condition of 5000 W net electric power out. As indicated in Table 1, the system includes a relatively large fuel cell stack with an area $A_{cell}$ = 300 cm$^2$ per cell and the number of cells, $n_{cells}$ = 75. Such a large stack is necessary to avoid the large anode overpotentials associated with non-zero CO concentrations at high current densities. This allows for adequate power densities to be achieved even for the baseline CO tolerance when anode inlet CO concentrations rise up to 200 ppm.

Full-power and half-power conditions over a range of $T_{amb}$ are used to characterize the performance of the baseline system in Fig. 3a, which presents overall system efficiency, $\eta_{th}$, and net water balance. Net water balance is based on water supplied to the fuel processor and water collected from the exhaust condenser and cathode condensate knockout, and its importance stems from portable or mobile applications where water supply will be in general limited to the water recovered from the system exhaust. The baseline system uses the current fuel cell CO-tolerance (derived from the curves in Fig. 2), coupled with PROx reactor performance at a baseline CO conversion of 0.95 and CO selectivity of 0.85. As expected, decreases in cooling and other BOP loads lead to slight increases in $\eta_{th}$ and more significant increases in net water balance with decreasing $T_{amb}$. In fact, the water balance reaches 0.0256 gmol s$^{-1}$ at full power conditions for $T_{amb}$ = 10 °C, which is off the scale in Fig. 3a. The results in Fig. 3a can be readily compared with the earlier study on a similarly sized, liquid-fueled PEM fuel cell system using a Pd membrane for $H_2$ purification and an anode recirculation loop for the stack fuel supply [15]. Unlike the previously reported system with the Pd membrane, positive net water balance for the system with PROx clean-up is achieved at ambient temperatures up to 50 °C. In fact, for all operable conditions explored in the current study with the ATR operation fixed at an $S/C$ of 1.6, positive water balance is achieved for the PEM fuel cell system with PROx reactor $H_2$ clean-up presented in this study.

It is interesting to note that $\eta_{th}$ for the current system at full power (24.8% at $T_{amb}$ = 30 °C) is lower than $\eta_{th}$ for the system with the Pd membrane at similar ATR conditions (26.8% at $T_{amb}$ = 30 °C [15]), but $\eta_{th}$ for the current system at half power is comparable for both systems (30.4 and 30.1%, respectively). The drop in $\eta_{th}$ at full power for the current system is due in part to the non-zero CO concentrations out of the PROx reactor substantially reducing the fuel cell stack voltage due to higher anode CO overpotentials at high current conditions and thus lowering stack efficiency at high power conditions. The drop in efficiency due to CO in the stack is also significant at the full power conditions because higher WGS reactor outlet temperatures at full power operating conditions result in higher CO concentrations into the PROx reactor and subsequently into the anode, which also leads to higher anode CO overpotentials. The drop in efficiency at full power is further detailed in the first two data columns in Table 2, which lists some key operating states for the full and half-power conditions at a baseline CO tolerance, including $V_{cell}$ and outlet CO concentrations from the WGS and PROx reactors. The drop of $V_{cell}$ by more than 0.1 V between half power and full power illustrates the impact of both the higher

**Table 2**
Key system states and outputs for two $\dot{W}_{net}$ baseline conditions from Table 1.

| Parameter | Value | | | |
|---|---|---|---|---|
| $\dot{W}_{net}$ (W) | 2500 | 5000 | 2500 | 5000 |
| Anode CO-tolerance factor, $\xi_{CO}$ | 1.0 | 1.0 | 5.0 | 5.0 |
| Overall system efficiency, $\eta_{th}$ | 0.304 | 0.248 | 0.312 | 0.295 |
| Individual cell voltage, $V_{cell}$ (V) | 0.755 | 0.619 | 0.773 | 0.718 |
| Average current density (A cm$^{-2}$) | 0.185 | 0.440 | 0.180 | 0.374 |
| Gross power demand, $\dot{W}_{gross}$ (W) | 3141 | 6137 | 3135 | 6047 |
| Net water balance (g s$^{-1}$) | 0.0107 | 0.0188 | 0.0105 | 0.0173 |
| ATR reactor outlet temperature, $T_{ref,out}$ (K) | 1010 | 1002 | 1014 | 1006 |
| WGS membrane reactor conditions | | | | |
| Outlet temperature, $T_{WGS,out}$ (K) | 497 | 625 | 493 | 607 |
| Outlet $H_2$ mole fraction | 0.408 | 0.397 | 0.408 | 0.401 |
| Outlet CO mole fraction | 0.0182 | 0.0291 | 0.0182 | 0.0250 |
| PROx reactor conditions | | | | |
| Outlet temperature after cooling, $T_{PROx,out}$ (K) | 333 | 345 | 333 | 339 |
| Outlet $H_2$ mole fraction, $X_{H_2,PROx,out}$ | 0.390 | 0.370 | 0.390 | 0.378 |
| Outlet CO concentration (ppm) | 63 | 247 | 61 | 178 |

current densities and anode inlet CO concentrations on fuel cell performance (efficiency).

To better understand the impact of different operating conditions on the complex system performance, it is helpful to consider how the overall system efficiency can be broken into subsystem efficiencies. The overall system efficiency $\eta_{th}$, is defined here by Eq. (1):

$$\eta_{th} = \left(\frac{\dot{W}_{net}}{\dot{m}_{HC,in} h_{HC,comb}}\right) = \left(\frac{n_{cells} A_{cell} i V_{cell} - \dot{W}_{lost}}{\dot{m}_{HC,in} h_{HC,comb}}\right) \quad (1)$$

where the work lost $\dot{W}_{lost}$ is due to parasitic loads and to motor and inverter inefficiencies. The first term in the right-hand-side numerator is the power produced by the PEM fuel cell stack.

The overall efficiency $\eta_{th}$ can be broken out into the product of subsystem efficiencies associated with the fuel processing and purification ($\eta_{FP}$), the fuel cell stack ($\eta_{FC}$), and the balance of plant ($\eta_{BOP}$). The equations for each of these efficiencies are provided here in Eqs. (2)–(4):

$$\eta_{FP} = \left(\frac{\dot{m}_{H_2,anode,in} h_{H_2,comb}}{\dot{m}_{HC,in} h_{HC,comb}}\right) \quad (2)$$

$$\eta_{FC} = \left(\frac{n_{cells} A_{cell} i V_{cell}}{\dot{m}_{H_2,anode,in} h_{H_2,comb}}\right) = \left(\frac{\varepsilon_{H_2,FC} 2F \bar{W}_{H_2} V_{cell}}{h_{H_2,comb}}\right) \quad (3)$$

$$\eta_{BOP} = \left(\frac{n_{cells} A_{cell} i V_{cell} - \dot{W}_{lost}}{n_{cells} A_{cell} i V_{cell}}\right) \quad (4)$$

The fuel processor efficiency, $\eta_{FP}$, is the ratio of combustion enthalpy in $H_2$ exiting the PROx reactor and entering the fuel cell stack to the combustion enthalpy of the hydrocarbon fuel consumed to produce the $H_2$. The fuel cell stack efficiency, $\eta_{FC}$, is the power produced by the fuel cell divided by the combustion enthalpy of $H_2$ entering the stack, including non-utilized hydrogen. Since the stoichiometric ratio of $H_2$ flow to $H_2$ consumed in the anode is fixed at 1.3 (as indicated in Table 1) for the power conditions in this study, the mass flow of $H_2$ into the anode is proportional to the current density. Thus, Eq. (3) can also be written in terms of fuel cell utilization $\varepsilon_{H_2,FC}$ (=0.77 for the fixed anode stoichiometric ratio), and this is shown in the right-hand-side expression. Finally, the balance of plant efficiency $\eta_{BOP}$ is the ratio of useable net power to the total power produced. It is readily seen that the product of Eqs. (2)–(4) produces the overall system efficiency in Eq. (1).

To understand the variations in $\eta_{th}$ shown in Fig. 3a and b plots the breakdown of the three subsystem efficiencies for the full and half-power cases over the range of $T_{amb}$. Increasing from half to full power results in significant decreases in $\eta_{FC}$, slight reductions in $\eta_{FP}$, and slight gains in $\eta_{BOP}$. The decrease in $\eta_{FP}$ with increasing $\dot{W}_{net}$ occurs at higher $T_{amb}$ and arises from the increased WGS outlet temperature, $T_{WGS,out}$, rising above the minimum WGS equilibrium temperature (575 K). The higher $T_{WGS,out}$ at the higher power conditions lowers $H_2$ (and raises CO) equilibrium outlet mole fractions as indicated in Table 2. The correlation between $\dot{W}_{net}$ and $T_{WGS,out}$ occurs because both ATR and WGS reactor heat losses (driven by both radiation and natural convection) do not scale proportionally with reactor flow rates. As the flow rate increases the constant reactor stoichiometry results in higher $T_{WGS,out}$ and thus somewhat lower $H_2$ content but higher CO content out of the WGS. The associated higher CO exiting the WGS at the higher $\dot{W}_{net}$ and $T_{WGS,out}$ also increases parasitic $H_2$ consumption in the PROx reactor, which causes further decreases in $\eta_{FP}$ with increasing $\dot{W}_{net}$. It should be noted that these effects could be mitigated by adjusting $S/C$ up and $O/C$ down with increased power conditions to encourage higher $H_2$ out of the WGS reactor, but such control strategies are outside the scope of this study which kept the $S/C$ and $O/C$ fixed for all power conditions.

The higher levels of CO out of the WGS and subsequently the PROx reactor with increasing $\dot{W}_{net}$ result in lower $V_{cell}$ due to higher anode overpotentials and thus lower $\eta_{FC}$, as clearly illustrated in Fig. 3b. The drop in $V_{cell}$ with increased power will occur even with pure $H_2$ feeds due to higher stack current densities, but the increased CO concentrations in the anode feed causes an even larger drop in $\eta_{th}$ with $\dot{W}_{net}$. Because balance of plant components such as compressors and fans are sized to meet maximum load and to run more efficiently near the full power output conditions, increases in balance of plant efficiency $\eta_{BOP}$ with increasing $\dot{W}_{net}$ can offset some of these losses in overall efficiency. However, at higher $T_{amb}$, parasitic loads associated with the coolant loop fan and pump grow substantially at full power condition and cause $\eta_{BOP}$ to decrease as seen in Fig. 3b. Since the fuel processor and fuel cell efficiencies are largely unaffected by $T_{amb}$, the drop in $\eta_{BOP}$ at the higher $T_{amb}$ results in an even larger drop in overall system efficiency as $\dot{W}_{net}$ increases.

The first exploration of the effects of enhanced CO tolerance involved rerunning the cases of Fig. 3 with the same PROx reactor settings but with a 5X increase in $\xi_{CO}$, the anode electrocatalyst CO tolerance. The $\eta_{th}$ and net water balance for the system with enhanced CO tolerance are plotted in Fig. 4a, and the subsystem efficiencies $\eta_{FP}$, $\eta_{FC}$ and $\eta_{BOP}$ are shown in Fig. 4b. With the same PROx conditions (CO conversion of 0.95 and CO selectivity of 0.85), the increased anode CO tolerance primarily serves to raise $V_{cell}$ and thus $\eta_{FC}$. These increases are much more significant at the full power conditions where CO anode overpotentials are much larger for the baseline condition. Whereas at the half-power conditions, low cur-

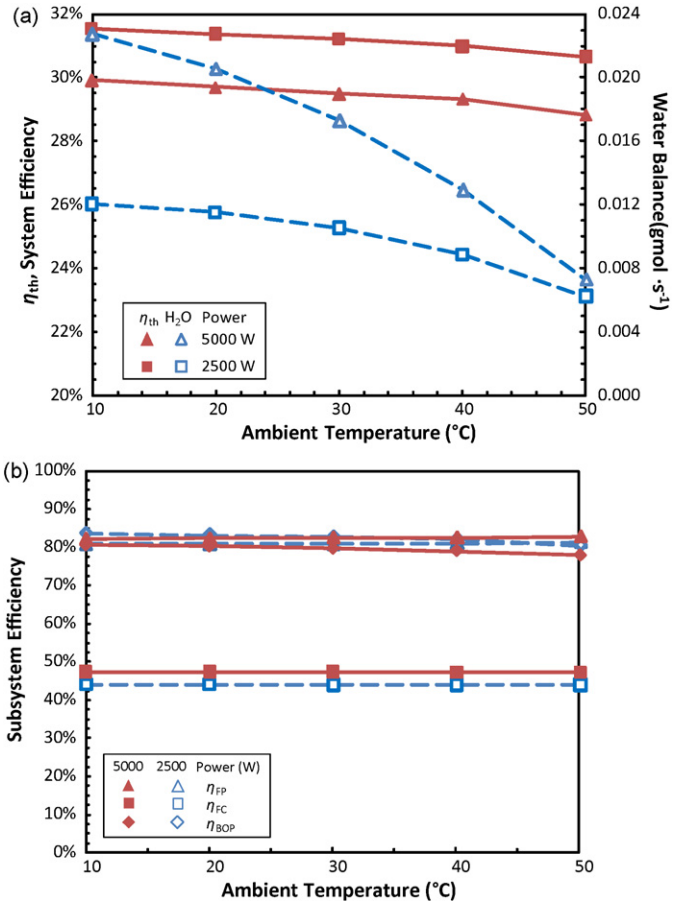


**Fig. 4.** PEM fuel cell performance vs. $T_{amb}$ at full and half power for a CO tolerance 5X the baseline and for PROx reactor performance at 95% CO conversion and 0.85 CO selectivity: (a) total system efficiency and net water balance, and (b) subsystem efficiencies (fuel processor, fuel cell stack, and balance of plant).

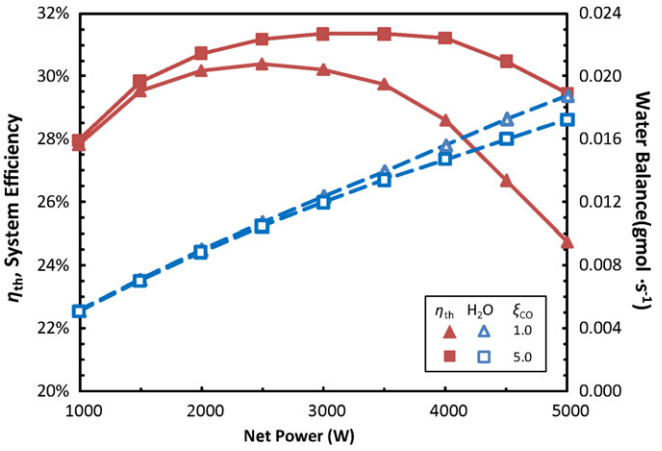


**Fig. 5.** System efficiency and water balance vs. total net power at $T_{amb}$ = 30 °C for baseline and 5X baseline CO tolerance with PROx reactor performance at 95% CO conversion and 0.85 CO selectivity.

rent densities and relatively low CO concentrations in the anode do not result in such large anode overpotentials, and thus, smaller improvements on the system efficiency are seen with increased $\xi_{CO}$. The significant improvement at full power conditions can be readily seen by comparing the full power $\eta_{th}$ vs. $T_{amb}$ curves in Figs. 3a and 4a. The increases in $\eta_{FC}$ (38.0–44.1% at $T_{amb}$ = 30 °C) for the full power conditions with the enhanced CO tolerance are seen by comparing Figs. 3b and 4b. On the other hand, the increases in $\eta_{FC}$ with $\xi_{CO}$ at half power (46.3–47.4% at $T_{amb}$ = 30 °C) are not so significant. The other two subsystem efficiencies, $\eta_{FP}$ and $\eta_{BOP}$, remain largely unaffected by $\xi_{CO}$. In general, over the entire $T_{amb}$ range, the increase in $\xi_{CO}$ from 1.0 to 5.0 (for the system at the baseline PROx reactor conditions) increases $\eta_{th}$ by 4.5–5.0% points or more at full power and only 0.8% points at half power. The water balance, for the most part, remains unchanged with the increase in $\xi_{CO}$.

It is worthwhile to explore how the trends observed above translate over a broader range of power conditions. Fig. 5 plots $\eta_{th}$ and net water balance at $T_{amb}$ = 30 °C as a function of $\dot{W}_{net}$ from 1000 to 5000 W for both $\xi_{CO}$ = 1 and 5. The plot shows that the significant improvements in $\eta_{th}$ with the higher $\xi_{CO}$ improving $V_{cell}$ and $\eta_{FC}$ taper off with decreasing power such that below half power the improvements are insignificant. This is because of the low CO overpotentials with the high baseline PROx conversion at the low power conditions and the limited impact at improving CO tolerance. As discussed later, reduced PROx CO conversion would cause the effects of increased $\xi_{CO}$ to be more significant at the low power conditions.

Another interesting feature in Fig. 5 is the peaking of $\eta_{th}$ for both $\xi_{CO}$ systems at intermediate powers ($\dot{W}_{net}$ between 2500 and 3500 W). The peak is due to the competing effects of decreasing $\eta_{BOP}$ and increasing $\eta_{FC}$ and $\eta_{FP}$ with decreasing $\dot{W}_{net}$. As the power decreases, the compressor and fan isentropic efficiencies decrease, and the fraction of power committed to parasitic loads $\dot{W}_{lost}$ increases causing a drop in $\eta_{BOP}$ (from 81.4% at full power to 70.0% at 1000 W for the baseline CO tolerance). The rise in $\eta_{FC}$ due to increases in $V_{cell}$ with reduced power demands does offset the trend in $\eta_{BOP}$, but at the lowest powers (<2500 W) the decrease in $\eta_{BOP}$ is more substantial than the increase in $\eta_{FC}$. The increase in $\eta_{FP}$ with reduced $\dot{W}_{net}$ and the associated decreases in reformer flows and $T_{WGS,out}$ (as discussed above) occurs until $T_{WGS,out}$ falls below the equilibrium temperature limit (573 K) such that no more improvements to $H_2$ mole fractions out of the WGS are achievable with the assumed kinetic limits of the WGS reactor. $T_{WGS,out}$ reaches its low-temperature equilibrium outlet at $\dot{W}_{net}$ = 3500 W and below that power output, further reductions in fuel flow do not lead to improvements in $\eta_{FP}$. All of the same trade-offs between decreasing $\eta_{BOP}$ and increasing $\eta_{FC}$ and $\eta_{FP}$ with decreasing $\dot{W}_{net}$ result in an optimal $\eta_{th}$ at the intermediate power conditions as illustrated in Fig. 5. Resizing of components such as the fuel cell stack or the cathode or ATR air compressors may shift the $\dot{W}_{net}$ values for optimal efficiency, but studying component size effects on system performance is saved for another study.

The link between $T_{WGS,out}$ and fuel cell operating conditions leads to interesting relationships in the system studied here. Because the WGS reactor is presumed to be large enough to achieve equilibrium down to as low as 300 °C, its outlet CO and $H_2$ concentrations will decrease and increase respectively with decreasing $T_{WGS,out}$ down to the 575 K limit as discussed earlier. However, below the equilibrium limit temperature, WSG outlet CO and $H_2$ concentrations and subsequent anode CO and $H_2$ inlet concentrations for fixed PROx will become relatively insensitive to WGS operating conditions. This is illustrated to some extent in Fig. 6 which plots anode inlet CO ppm vs. $T_{WGS,out}$ in K for a range of power conditions and two different $\xi_{CO}$. As $T_{WGS,out}$ increases above 575 K anode inlet CO ppm rises sharply. This rise in CO concentrations is accompanied by a drop in $V_{cell}$ also plotted in Fig. 6 vs. $T_{WGS,out}$. The results in Fig. 6, however, show that as the anode inlet CO ppm rises with increasing $T_{WGS,out}$, the impact of improved anode CO tolerance on $V_{cell}$ also becomes more significant. These results indicate the importance of optimizing WGS performance when using PROx clean-up and the potential for improved CO-tolerant anode electrocatalysts in reducing the demands on the WGS reactor (in terms

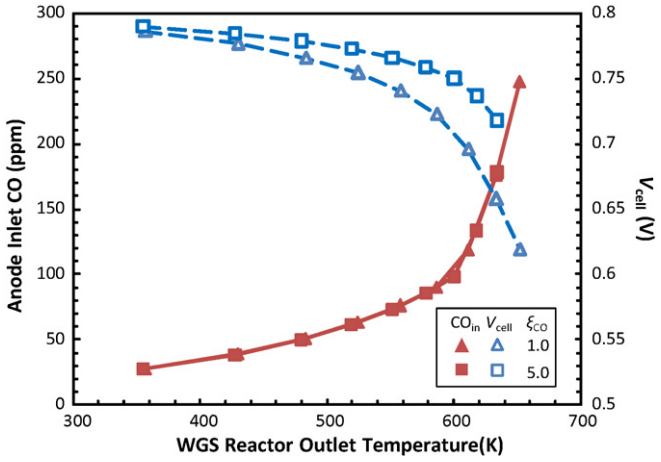


**Fig. 6.** Anode inlet CO ppm and $V_{cell}$ for the stack vs. water-gas-shift outlet temperature for a range of power conditions (1000–5000 W) for the baseline and 5X the baseline CO tolerance. PROx reactor performance is at 95% conversion and 0.85 CO selectivity.

of size) and perhaps also the PROx reactor as discussed further below.

To explore the effects of power demand and $\xi_{CO}$ on the balance of plant more fully, the specific parasitic power demands for the system over a range of $T_{amb}$ are shown in Fig. 7, both for baseline and 5X-increased anode CO tolerance at full power (left-hand side) and half power (right-hand side). In general, the total parasitics $\dot{W}_{lost}$ for full and half power for the different CO tolerances are less than 20% of net power out. The results in Fig. 7 show that the largest parasitic losses come from the cathode and fuel processor (FP) compressors. The radiator fan power demand increases with $T_{amb}$, rising sharply at full power as $T_{amb}$ approaches the temperature of the coolant (70 °C) and the fan must push significantly more air through the coils to achieve adequate cooling for the coolant loop and the exhaust condenser. Parasitic loads do not scale linearly with net power, resulting in lower $\eta_{BOP}$ at the lower power output as discussed in conjunction with Fig. 5 above.

The results from Figs. 3–7 suggest that increasing CO tolerance without changing PROx reactor conditions provides significant improvements in overall system performance only at conditions

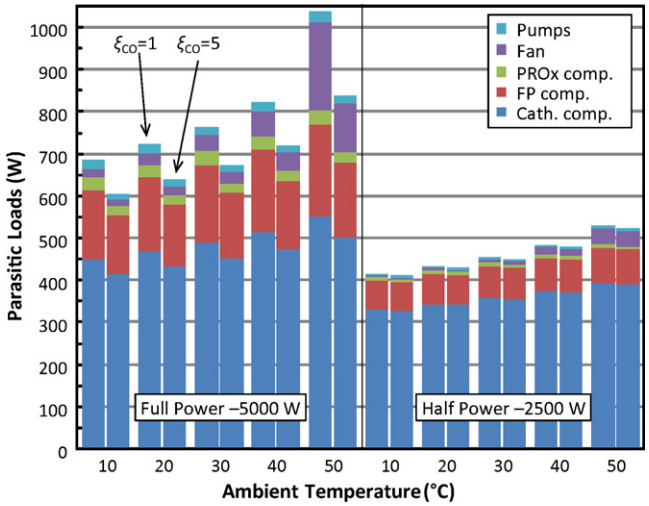


**Fig. 7.** Comparison of parasitic loads at full and half power for a range of $T_{amb}$ with the baseline CO tolerance (left bar of each pair) and 5X the baseline CO tolerance (right bar of each pair). PROx reactor performance is at 95% conversion and 0.85 CO selectivity.

where anode overpotentials due to CO are relatively large. However, the baseline PROx reactor represents a very high-performance reactor with high CO conversion (95%) and high CO selectivity (85%). Such high performance with good temperature control may require large, expensive multi-stage reactors and heat exchangers. As such, it is worth investigating whether increased CO tolerance might allow for less expensive PROx reactors with either reduced conversion (smaller size) and/or reduced selectivity (less expensive catalysts). The first parametric study thereunto investigated the impact of varying PROx selectivity while keeping PROx CO conversion high at the baseline 95%. For selectivities lower than the baseline value of 0.85, increased $H_2$ consumption in the PROx will decrease system efficiency primarily through $\eta_{FP}$—by increasing the amount of fuel required ($\dot{m}_{HC,in}$) to produce the same amount of $H_2$ ($\dot{m}_{H_2,anode,in}$) for the stack. Reduced selectivities will also result in minor reduction in $\eta_{BOP}$ – by increasing the PROx compressor loads and in $\eta_{FC}$ – by decreasing the $H_2$ mole fraction in the anode feed. These combined effects on overall system efficiency are illustrated in the $\eta_{th}$ vs. CO selectivity curves shown in Fig. 8 for full power conditions at $T_{amb}$ = 30 °C. Although PROx CO selectivity does not have a direct or large impact on CO concentrations into the anode (also shown in Fig. 8), reduced CO selectivity lowers $V_{cell}$ and thus $\eta_{FC}$ because of the increased $H_2$ loss in the PROx reactor. Because $\eta_{th}$ is a strong function of CO selectivity, it shows the value in continued research activity to develop improved, reliable PROx catalysts.

Over the entire range of PROx selectivities (0.75–1.00) investigated, a 5X improvement in $\xi_{CO}$ provides almost 5.0% points improvement in $\eta_{th}$ for full power conditions. This significant improvement with increased $\xi_{CO}$ is due principally to the improvements in $\eta_{FC}$ with the reduced anode overpotentials as stated before. The additional minor effects to improve $\eta_{BOP}$ and $\eta_{FP}$ as discussed in conjunction with Fig. 4 also apply over the range of conditions plotted in Fig. 8. With decreasing CO selectivity, increased anode overpotentials allow for increased $\xi_{CO}$ to impact $V_{cell}$ and thus $\eta_{FC}$ and $\eta_{th}$ more significantly in a positive way. This is borne out by the results in Fig. 8 which shows approximately 4.8% points improvement in $\eta_{th}$ at the 0.75 selectivity. This improvement drops to 4.6% points for the idealized CO selectivity of 1.0.

Changes in PROx selectivity require changes in catalyst composition, but changes in PROx CO conversion can be accomplished with only changes in catalyst loading and thus may be a straightforward means of impacting system performance and/or cost. A reduced PROx catalyst loading may allow for fewer PROx reactor

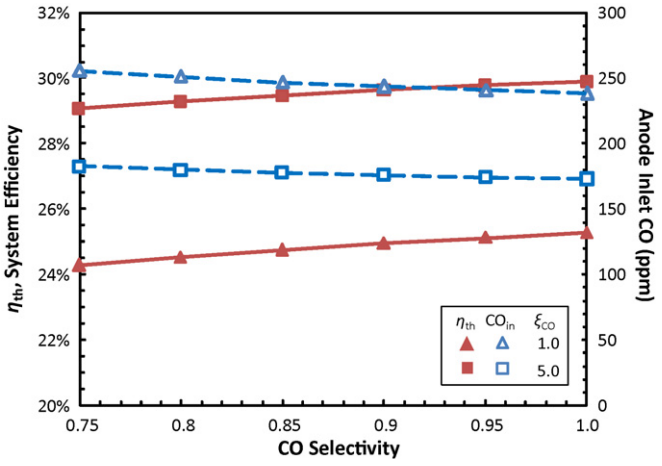


**Fig. 8.** Full power (5000 W) system efficiency and anode inlet CO ppm at $T_{amb}$ = 30 °C for varying PROx reactor CO selectivities with constant PROx reactor CO conversion at 95% for baseline at 5X baseline CO tolerances.

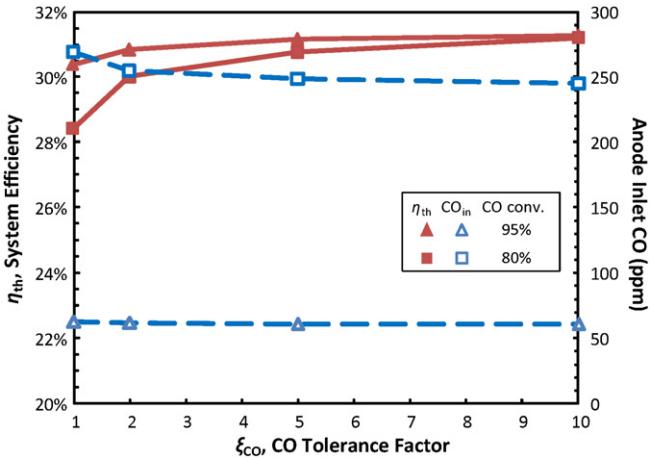


**Fig. 9.** Total system efficiency and anode inlet CO ppm vs. anode electrocatalyst CO tolerances at half power for PROx reactors with 80% and 95% CO conversion at a constant 0.85 CO selectivity.

stages and reduced system cost and size. The question then arises as to how potential improvements in CO tolerance of anode electrocatalysts can reduce the demand for such high PROx conversions while maintaining adequately high $\eta_{th}$. To explore such issues, $\xi_{CO}$ was varied from 1 to 10 for two different PROx CO conversions (the baseline 95% and a reduced 80%). First explored are half-power conditions, where the high baseline PROx conversion of 95% shows very minor improvements in $\eta_{th}$ with increased $\xi_{CO}$. When the PROx reactor is shrunk such that CO conversion is only 80%, $\eta_{th}$ drops by 2% points from 30.4 to 28.4%. However, as shown in Fig. 9, increasing $\xi_{CO}$ to higher values reduces this penalty for the reduced PROx conversion at half power, such that by $\xi_{CO} = 5.0$, the drop in $\eta_{th}$ is less than 0.5% points from 31.2 to 30.8% and by $\xi_{CO} = 10.0$, the drop in $\eta_{th}$ is less than 0.1% points. These improvements in performance which are principally tied back to improvements in $\eta_{FC}$ illustrate one of the real system values in improving anode CO tolerance. Higher fuel cell CO tolerance allows for reduction in demands for CO clean-up and for PROx-based clean-up as studied here, this can mean smaller, less complex reactors with lower CO conversion.

The value of higher $\xi_{CO}$ on allowing lower PROx reactor performance is further illustrated in Fig. 10a by plotting $\eta_{th}$ as well as anode inlet CO ppm for full power conditions with PROx CO conversions of 80 and 95%. The improvements in $\eta_{th}$ with increased CO for both PROx CO conversions are much more dramatic at the full power conditions because of the higher anode overpotentials with more potential for increasing $V_{cell}$ and $\eta_{FC}$ with higher $\xi_{CO}$. For the baseline 95% conversion, $\eta_{th}$ at full power increases more significantly up to $\xi_{CO} = 5.0$ and less so as $\xi_{CO}$ increases beyond 5.0. This is in large part because the sub-100 ppm CO entering the anode for the higher PROx conversion remains largely insensitive to $\xi_{CO}$, and so there is limited margin for further improvement at the highest values of $\xi_{CO}$ studied. On the other hand, for the reduced (80%) PROx CO conversion cases, increases in $\eta_{th}$ with $\xi_{CO}$ remain large even up to $\xi_{CO} = 10.0$. This is in part because the lower CO results in quite high CO concentrations entering the anode, and these concentrations drop dramatically as $\xi_{CO}$ rises. In fact, the CO concentrations become so high (>2000 ppm) at the baseline $\xi_{CO}$ for PROx conversion of 80% that the fuel cell system is unable to produce the full power $\dot{W}_{net} = 5000$ W, as indicated by no point for this case in Fig. 10a. However, for $\xi_{CO} = 2.0$, $\eta_{th}$ reaches 20.8% with the reduced PROx conversion and this values rises significantly to 28.1% as $\xi_{CO}$ is increased to 10.0. This is in large part because of the significant improvements in $\eta_{FC}$ under these conditions where CO overpotentials at the baseline conditions are exceptionally large without the enhanced anode CO tolerance. $V_{cell}$ is 0.529 V at the

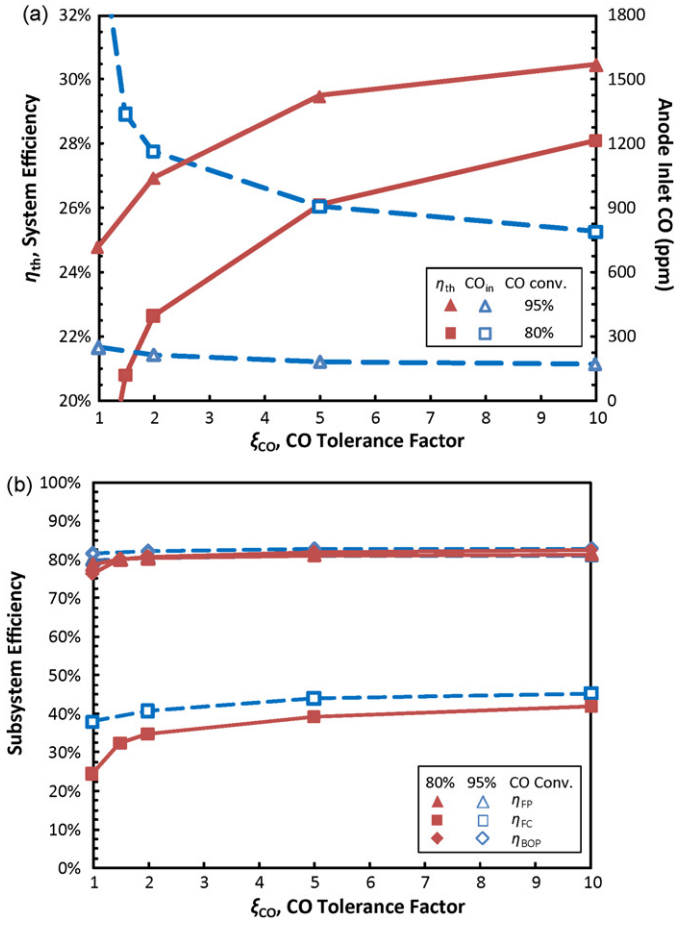


**Fig. 10.** PEM fuel cell performance vs. anode electrocatalyst CO tolerances at full power for PROx reactors with 80 and 95% CO conversion at a constant 0.85 CO selectivity: (a) total system efficiency and anode inlet CO ppm and (b) subsystem efficiencies.

$\xi_{CO} = 2.0$ condition and rises to a much more acceptable value of 0.682 V at $\xi_{CO} = 10.0$ for the 80% PROx conversion cases. The impact of $\xi_{CO}$ on $\eta_{FC}$ is illustrated in Fig. 10b which breaks out the subsystem efficiencies and shows the significant increase in $\eta_{FC}$ with $\xi_{CO}$ for the lower PROx CO conversion cases. It is noteworthy that the significant improvement in $\eta_{FC}$ also results in smaller improvements in both $\eta_{BOP}$ and $\eta_{FP}$ by reducing the compressor and fan flow requirements and by also improving WGS outlet equilibrium with lower CO and higher $H_2$ concentrations. These results clearly indicate that the value of improved anode CO tolerance is tightly linked to the performance of the PROx reactor. As such, the advantages of enhanced CO tolerance depend on the system and its range of operating conditions.

## 5. Conclusion

This study provides a preliminary exploration into the benefits of improving anode CO tolerance on the system performance of a liquid hydrocarbon-fueled PEM fuel cell generator (with 5000 W maximum net power) using a PROx reactor for reformate clean-up. A system model was built which included empirical curves for baseline CO tolerance based on testing of state-of-the-art PtMo anode catalysts in membrane electrode assemblies with low-temperature Nafion membranes. A CO-tolerance factor was defined which shifted the polarization effects of CO to higher ppm values. The system model provided a basis for exploring the interactions between CO tolerance of the anode and PROx operating conditions.

For the current study, overall system efficiencies at baseline CO tolerances and state-of-the-art PROx reactor performance (95% CO conversion at 85% CO selectivity) ranged from 24.8% at full power ($\dot{W}_{net} = 5000$ W) up to 30.4% at intermediate power conditions ($\dot{W}_{net} = 2500$ kW). At lower power conditions, efficiencies dropped off due to increases in the fraction of work required to operate balance of plant compressors, fans, and pumps. With advances in CO-tolerant catalyst to 5X reduction in CO penalties, model calculations show that the fuel cell efficiencies increase only slightly at the lower power conditions to 31.2% at $\dot{W}_{net} = 2500$ W, but more dramatically at high power conditions to 29.5% at $\dot{W}_{net} = 5000$ W. In general, conditions for significant improvement in system efficiency with increased anode CO tolerance are those where relatively high current densities and relatively high (>50 ppm) anode inlet CO concentrations cause large anode overpotentials that can be reduced with improved CO-tolerant anode electrocatalysts. Improvement in fuel cell voltages and efficiencies with increased CO tolerance has additional system benefits such as small reductions in parasitic loads which can further increase system efficiencies. Furthermore, increased fuel cell CO tolerance can permit significantly lower PROx conversion without the significant penalty in overall system efficiency observed at baseline tolerance. Further studies with alternative system operating conditions can explore how advances in CO-tolerant anode electrocatalysts provide opportunities for reducing system costs with smaller PROx or WGS reactors as well as potentially smaller fuel cell stacks. Such a study may reveal opportunities for PEM fuel cell systems with CO-tolerant anodes to compete effectively for portable and/or distribute power applications involving liquid hydrocarbon fuels.

## Acknowledgments

The authors would like to acknowledge the generous support of the Army Research Lab under contract number W911QX-07-C-0089 (Dr. Deryn Chu–program manager). The authors also acknowledge the collaboration with Dr. Zhufang Liu and Prof. Bryan Eichhorn at the University of Maryland for helping to fabricate and characterize the CO-tolerant electrocatalysts used for the curves in Fig. 2. Conversations with Pat Hearn of Ballard Power Systems were helpful in the model validation.

## References

[1] M.J. Castaldi, F. Barrai, Catalysis Today 129 (2007) 397–406.
[2] S. Specchia, A. Cutillo, G. Saracco, V. Specchia, Industrial & Engineering Chemistry Research 45 (2006) 5298–5307.
[3] S.K. Kamarudin, W.R.W. Daud, M.A. Som, M.S. Takriff, A.W. Mohammad, Journal of Power Sources 157 (2006) 641–649.
[4] W.H.H. Zhu, R.U. Payne, B.J. Tatarchuk, Journal of Power Sources 156 (2006) 512–519.
[5] J.R. Lattner, M.P. Harold, International Journal of Hydrogen Energy 29 (2004) 393–417.
[6] S. Alayoglu, A.U. Nilekar, M. Mavrikakis, B. Eichhorn, Nature Materials 7 (2008) 333–338.
[7] Z.F. Liu, E.T. Ada, M. Shamsuzzoha, G.B. Thompson, D.E. Nikles, Chemistry of Materials 18 (2006) 4946–4951.
[8] S. Mukerjee, R.C. Urian, S.J. Lee, E.A. Ticianelli, J. McBreen, Journal of the Electrochemical Society 151 (2004) A1094–A1103.
[9] R.J. Stanis, M.C. Kuo, J.A. Turner, A.M. Herring, Journal of the Electrochemical Society 155 (2008) B155–B162.
[10] M.V. Martinez-Huerta, J.L. Rodriguez, N. Tsiouvaras, M.A. Pena, J.L.G. Fierro, E. Pastor, Chemistry of Materials 20 (2008) 4249–4259.
[11] S. Ahmed, J. Kopasz, R. Kumar, M. Krumpelt, Journal of Power Sources 112 (2002) 519–530.
[12] R.M. Biesheuvel, G.J. Kramer, Journal of Power Sources 138 (2004) 156–161.
[13] E.D. Doss, R. Kumar, R.K. Ahluwalia, M. Krumpelt, Journal of Power Sources 102 (2001) 1–15.
[14] R.K. Ahluwalia, E.D. Doss, R. Kumar, Journal of Power Sources 117 (2003) 45–60.
[15] J.B. Pearlman, A. Bhargav, E.B. Shields, G.S. Jackson, P.L. Hearn, Journal of Power Sources 185 (2008) 1056–1065.
[16] K. Sasaki, K. Watanabe, Y. Teraoka, Journal of the Electrochemical Society 151 (2004) A965–A970.
[17] I. Kang, J. Bae, S. Yoon, Y. Yoo, Journal of Power Sources 172 (2007) 845–852.
[18] N. Maeda, T. Matsushima, H. Uchida, H. Yamashita, M. Watanabe, Applied Catalysis A-General 341 (2008) 93–97.
[19] P. Berg, A. Novruzi, K. Promislow, Chemical Engineering Science 61 (2006) 4316–4331.
[20] Z. Liu, J.E. Hu, Q. Wang, K.J. Gaskell, A.I. Frenkel, B.W. Eichhorn, Journal of American Chemical Society 131 (2009) 6924–6925.
[21] J.E. Hu, 'CO Tolerance of Nano-Architectured Pt-Mo Anode Electrocatalysts for PEM Fuel Cell Systems', M.S. Thesis, University of Maryland, College Park, MD, 2009.